ACS APPLIED MATERIALS & INTERFACES

Research Article

www.acsami.org

Strong Photocurrent from Two-Dimensional Excitons in Solution-Processed Stacked Perovskite Semiconductor Sheets

Shahab Ahmad,[*,†,‡] Pawan K. Kanaujia,[†] Harry J. Beeson,[§] Antonio Abate,[§] Felix Deschler,[§] Dan Credgington,[§] Ullrich Steiner,[§,∥] G. Vijaya Prakash,[*,†] and Jeremy J. Baumberg[*,‡]

[†]Nanophotonics Laboratory, Department of Physics, Indian Institute of Technology Delhi, New Delhi 110 016, India

[‡]Nanophotonics Centre and [§]Optoelectronics Group, Cavendish Laboratory, University of Cambridge, CB3 0HE Cambridge, U.K.

[∥]Adolphe Merkle Institute, University of Fribourg, Chemin des Verdiers 4, CH-1700 Fribourg, Switzerland

Supporting Information

ABSTRACT: Room-temperature photocurrent measurements in two-dimensional (2D) inorganic–organic perovskite devices reveal that excitons strongly contribute to the photocurrents despite possessing binding energies over 10 times larger than the thermal energies. The p-type $(C_6H_9C_2H_4NH_3)_2PbI_4$ liberates photocarriers at metallic Schottky aluminum contacts, but incorporating electron- and hole-transport layers enhances the extracted photocurrents by 100-fold. A further 10-fold gain is found when TiO_2 nanoparticles are directly integrated into the perovskite layers, although the 2D exciton semiconducting layers are not significantly disrupted. These results show that strong excitonic materials may be useful as photovoltaic materials despite high exciton binding energies and suggest mechanisms to better understand the photovoltaic properties of the related three-dimensional perovskites.

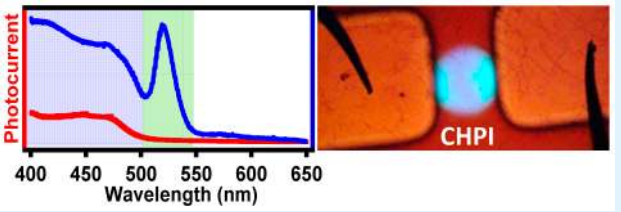

KEYWORDS: *inorganic–organic hybrid, layered perovskite, room-temperature exciton, exciton photocurrent, photodetector*

INTRODUCTION

Recently, lead halide based inorganic–organic (IO) hybrid perovskite materials have emerged as one of the most promising absorber materials for solar cells. Among these perovskites, in particular, the three-dimensional (3D) perovskite materials $CH_3NH_3PbI_3$ and $CH_3NH_3PbI_{3-x}Cl_x$ have been studied as photoresponsive materials in dye-sensitized architectures.[1−7] The power conversion efficiencies (PCEs) have seen unprecedented growth from below 10% in 2012[1,2] to above 20% by the end of 2014,[3,4] owing to excellent light-harvesting capabilities over the visible-to-near-IR spectrum due to the narrow band gap (1.5 eV). In 3D perovskite-based solar cells, it is predominantly free charge carriers that are generated and are responsible for the photovoltaic operation rather than the excitons (which have a binding energy of ∼50 meV).[8] However, the related series of two-dimensional (2D) perovskites possess much stronger 2D excitons and are thus normally considered to be of little use for light harvesting. Here we study the photovoltaic properties of 2D perovskites and show that, despite severe barriers to carrier transport between layers, the excitons are efficient light harvesters.

The 2D perovskites are part of the generic family of metal–organic frameworks with well-organized structural properties,[9,10] represented by the general formula $(RNH_3)_2MX_4$ where R is an organic cation, M is a divalent metal (such as Pb^{2+}, Sn^{2+}, Hg^{2+}, etc.), and X is a halogen (such as I^-, Br^-, or Cl^-). The basic crystal packing of these hybrids is a naturally self-assembled layered structure, where single sheets of corner-shared MX_6 octahedra and bilayers of organic cations are stacked alternately along the c axis (Figure 1a).[11−14] The interlayer separation and thickness of the inorganic layers can be controlled through the choice of amine-based organic cations.[15] The spatial quantum confinement of the 2D sheets leads to strongly bound excitons because of large differences in the band gaps of inorganic (∼2 eV) and insulating organic (∼4 eV) layers as well as their large dielectric mismatch ($\varepsilon_{org} < \varepsilon_{inorg}$).[16] The binding energy E_B of the Wannier–Mott excitons in 2D perovskite systems thus ranges from 200 to 300 meV.[17−22]

Such tightly bound excitons are difficult to dissociate into free charge carriers at room temperature (because $E_B \sim 10k_BT$), and hence free charge carriers are not likely to reach the electron/hole selective contacts. However, our data here clearly show that this is not generally the case and that, by the incorporation of suitable electron and hole conducting layers, the transport of excitons across the heterojunction can be manipulated. The purpose of the present study is to explore the photoresponse in 2D perovskites and understand this induced carrier transport. Our work suggests pathways to new device structures and opens possibilities for the further optimization of devices and photovoltaic functionality.

Received: July 31, 2015
Accepted: October 26, 2015
Published: October 26, 2015

DOI: 10.1021/acsami.5b07026
ACS Appl. Mater. Interfaces 2015, 7, 25227−25236

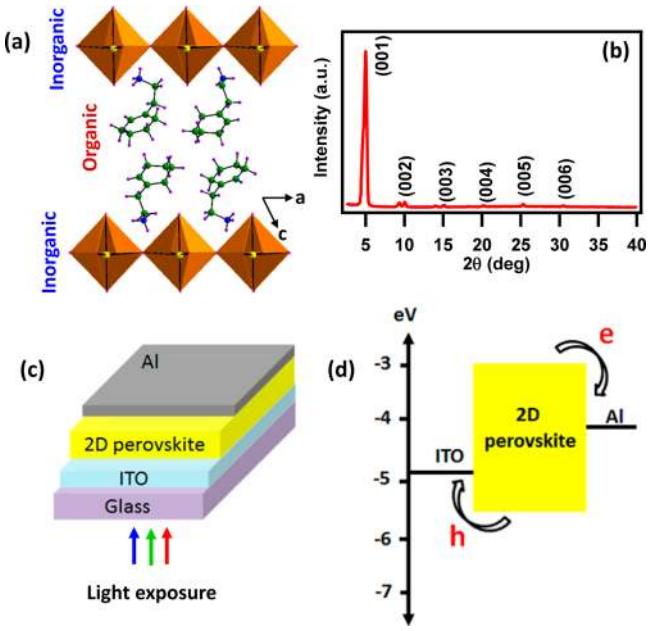

Figure 1. (a) Schematic crystal structure of 2D perovskite $(C_6H_9C_2H_4NH_3)_2PbI_4$.[14] (b) X-ray diffraction pattern of a CHPI thin film revealing a 2D-layered arrangement. (c) Schematic and (d) corresponding band diagram of the photodetector configuration **1** [Al/CHPI/ITO].

EXPERIMENTAL SECTION

Fabrication. To study the photocurrent properties in detail, three different device configurations are fabricated. In each case, the 2D IO perovskite $(C_6H_9C_2H_4NH_3)_2PbI_4$ (hereafter CHPI) is used as the photoresponsive material. For "base" configuration **1** (see Methods in the Supporting Information), CHPI is spun onto an indium tin oxide (ITO) anode and overcoated with evaporated aluminum or gold [Al/CHPI/ITO or Au/CHPI/ITO] (Figure 1c). The fabrication details of other configurations, **2** [Au/HTL/CHPI/c-TiO_2/FTO] and **3** [Au/HTL/CHPI/mp-TiO_2/c-TiO_2/FTO], are shown in the Supporting Information (see Methods). The effective area of all fabricated configurations is fixed to 9 mm^2.

Characterization. Spectral and transient photocurrent measurements are carried out using a potentiostat (Autolab and/or Ivium compactstat.e) and xenon lamp source (Bentham, 75 W) coupled to a monochromator (TMc 300, Bentham). To perform power-dependent photocurrent measurements, a 410 nm diode laser (~100 mW, continuous wave) is used separately in the same setup. A Leo variable-pressure scanning electron microscope is used for cross-sectional scanning electron microscopy (SEM) images of configurations **2** and **3**.

RESULTS AND DISCUSSION

Room-Temperature Exciton Photocurrent Response of 2D Perovskites. We first study the photogenerated charge-carrier properties of the 2D perovskite CHPI, in configuration **1**, without any electron- and hole-transport materials. In CHPI, the alternating stacks of 2D organic and inorganic layers (*c*-oriented) resemble natural multiple-quantum-well (MQW) structures (Figure 1a,b). The lowest-energy excitons reside in the inorganic MQW sheets and are stable at room temperature with large 300 meV binding energy.[10,23−30] The transient photocurrent response is observed upon room-temperature illumination through the transparent ITO electrode (Figure 1c). To identify the origin of the photocurrent, spectral scans are measured over a wide wavelength range from 210 to 1100 nm (Figure S1a in the Supporting Information). Figure 1d represents the energy-level diagram of configuration **1**.

The photocurrent spectral response of CHPI in configuration **1** is compared with the absorption and photoluminescence (PL) spectra of a bare CHPI film (Figure 2a). The origin of this photocurrent can be explained by considering the energy-level diagram (Figure 2b). Essentially the response is comprised of two regions: (a) a broad response from 300 to 475 nm and (b) a strong narrow exciton band peaking at 521 nm [with full width at half-height (fwhm) = 20 nm]. The broad region can be directly correlated to the band-to-band (BB) and charge-transfer (CT) absorption transitions (Figure 2b), and indeed the band edge from the photocurrent (2.46 eV) closely matches the optical absorption band edge. Absorbed photons generate charge carriers in the perovskite material, and the built-in potential at the Schottky interfaces (perovskite−metal and ITO−perovskite) allows collection of photogenerated carriers at the respective electrodes (Figure 1d).[31,32] Similarly, the narrow photocurrent band at 521 nm matches the exciton peak in absorption and is attributed to bound excitons (Figure 2a). The 10 nm red shift of the photocurrent peak from the absorption peak arises partly because the absorption depth (<100 nm) is shorter than the CHPI thickness (~800 nm),[23] so that only the longer wavelengths can generate excitons near the CHPI−metal contact. However, additional dissociation energies as well as thermalization effects are involved,[33] depending on the carrier mobilities and metal work functions.

The observation of such spectrally narrow strong exciton-related photocurrents at room temperature is unusual in

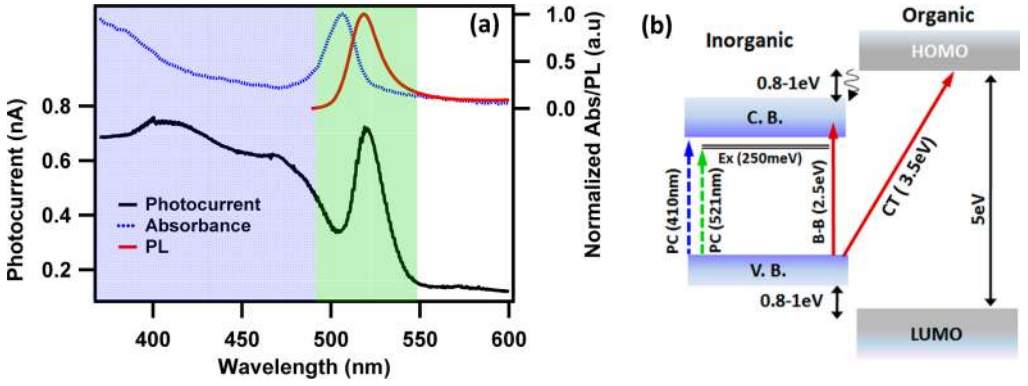

Figure 2. (a) Comparison of the photocurrent spectrum (1 V bias) with the absorption and PL spectra of a bare CHPI thin film. (b) Schematic energy-level band diagram indicating the BB, CT, and exciton bands within the inorganic and organic moieties of a 2D IO perovskite, CHPI.

DOI: 10.1021/acsami.5b07026
ACS Appl. Mater. Interfaces 2015, 7, 25227−25236

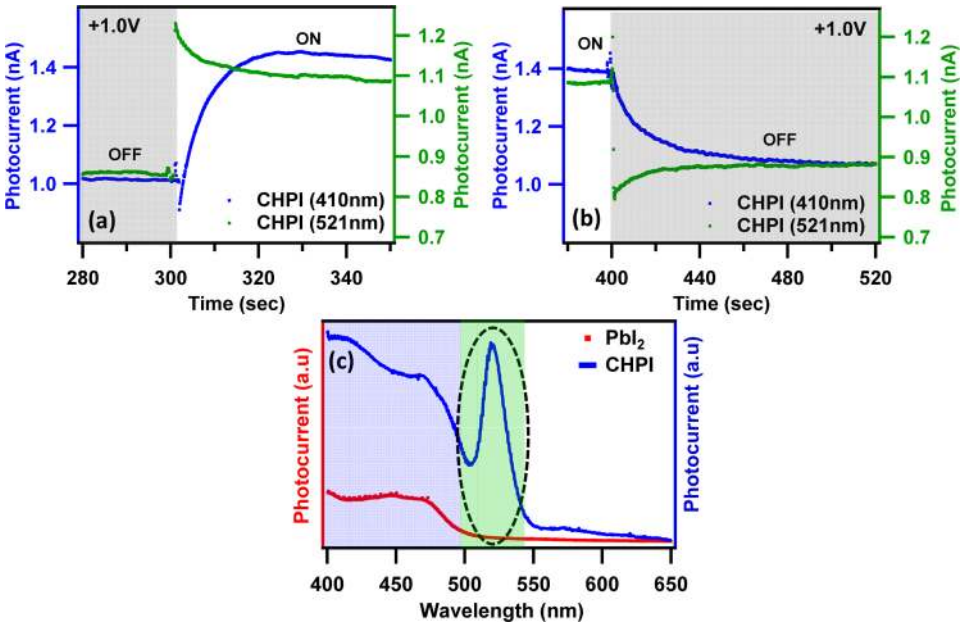

Figure 3. Transient photocurrent response of CHPI in configuration **1** showing (a) rise and (b) fall time profiles with the BB or CT region (410 nm) and exciton (521 nm) illumination under +1 V bias. Shaded regions show when the laser is OFF. (c) Comparison of room-temperature photocurrent spectral responses in CHPI and parent PbI_2 thin films.

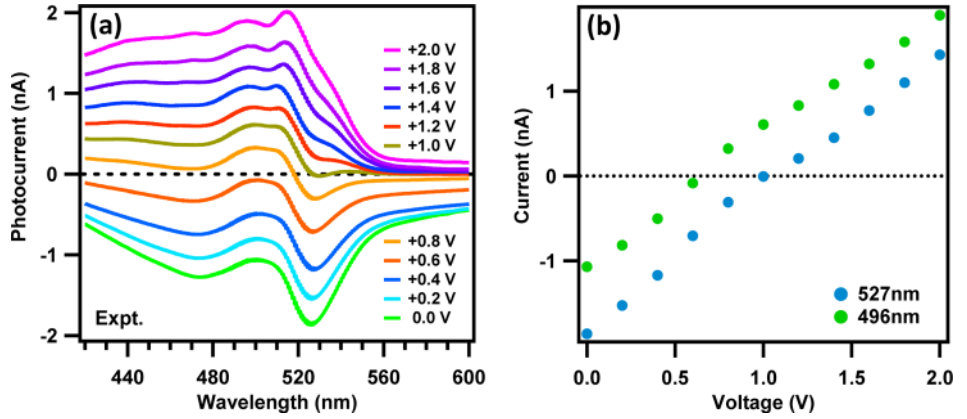

Figure 4. (a) Photocurrent spectral response with respect to the applied bias voltage for configuration **1**. (b) Variation of the photocurrent magnitudes with applied bias at specific wavelengths extracted from part a.

solution-processed semiconductor films. One puzzle is how excitons trapped on individual sheets, which are separated by high insulating barriers, can lead to photocurrent. Mitzi et al. studied inorganic–organic field-effect transistors (IOFETs) of spin-coated 2D perovskite films $[(C_6H_5C_2H_4NH_3)_2SnI_4]$, showing that the geometry of well-separated inorganic sheets is ideal for lateral charge transport, which depends on the size of the grains in the polycrystalline film.[11,34] This is less relevant when vertical transport across the layers is required as it is here, unless polycrystalline misorientation leads to interlayer conduction at grain boundaries. Hence, morphology effects must play a crucial role in the transport of charge carriers in such polycrystalline-layered materials.

The room-temperature transient photocurrent response is further investigated by measuring its dynamics within both the BB (410 nm) and exciton (521 nm) regions. The IO perovskite exhibits a much faster (100-fold) rise in the photocurrent upon exciton illumination at 521 nm (Figure 3a) compared to that upon BB (410 nm) illumination. Similarly, much faster photocurrent decay is visible from 521 nm illumination compared to 410 nm illumination (Figure 3b). Because similar photocurrent magnitudes are generated under 410 and 521 nm excitation and the absorptions are similar, this suggests that both photocarrier species contribute equally to the photocurrents measured in these 2D IO perovskites when fabricated in configuration **1**. However, distribution of the photocarriers and excitons may be rather different in the two situations, and most likely excitons are field-ionized in the immediate vicinity of the contacts (see below).

The influence of quantum and dielectric confinement can be further investigated by comparing the photocurrents from CHPI and the parent PbI_2 compound, integrated as a film within the same photodetector configuration. This parent network PbI_2 material is also a layered direct-band-gap semiconductor ($E_g \sim 2.55$ eV), with a layer-to-layer separation of ~7 Å.[35] During the formation of CHPI, PbI_2 structurally exfoliates as the organics intercalate inside the PbI_4^{2-} extended network, increasing the layer spacing to >20 Å.[36] Because the exciton binding energies are substantially lower (~30 meV) in the parent PbI_2, the optical exciton features are only observed

DOI: 10.1021/acsami.5b07026
ACS Appl. Mater. Interfaces 2015, 7, 25227–25236

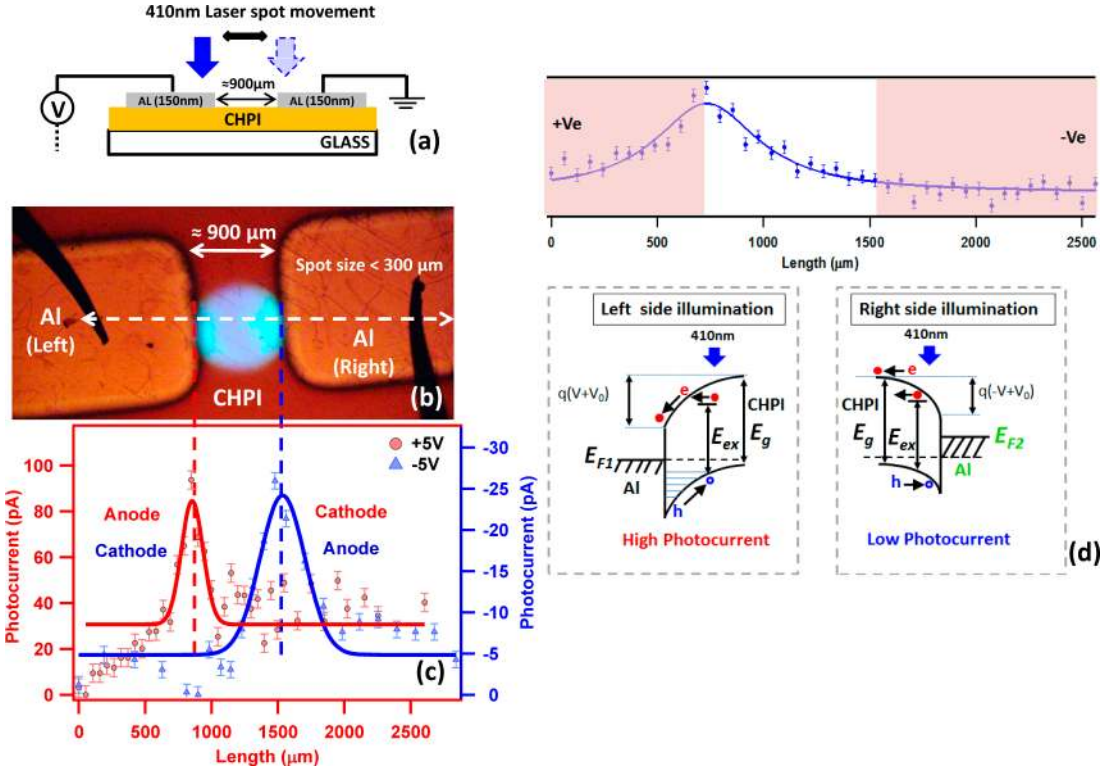

Figure 5. (a) Lateral-geometry Al/CHPI/Al photocurrent configuration fabricated on a glass substrate in (b) a bright-field image. Greenish-blue emission between the two aluminum contacts is luminescence ($\lambda_{em} \sim 520$ nm) due to 410 nm laser spot irradiation as well as laser scattering. (c) Scanning photocurrent response moving between aluminum contacts, at applied biases of +5 and −5 V. (d) Schematic energy band diagrams of Al/CHPI/Al under +5 V applied bias showing the band bending and photocarrier transport due to light irradiation at the left (+ve) and right (−ve) terminals.

at low temperature.[37] Room-temperature photocurrent measurements are performed on samples with PbI_2 films as the active layer [Al/PbI_2/ITO] and compared to CHPI (Figure 3c). Both devices exhibit a broad photocurrent response in the energy region (400−500 nm) associated with BB transitions.[38,39] However, unlike CHPI, photocurrent spectra of the PbI_2 films do not show any signature of the excitonic features near 521 nm. This experiment confirms the surprising result that the narrow photocurrent peak in CHPI at 521 nm originates solely from photocarriers associated with exciton transitions in the 2D organic−inorganic perovskite well structures. We also confirm that the photocurrent is linear in illumination power (Figure S1b in the Supporting Information), with only a weak nonlinear component, suggesting that no cooperative mechanism is involved.[40]

To explore the competing roles of electron−hole photocarriers and exciton photocurrents, the bias-dependent response is studied in configuration **1** at room temperature, up to +2.0 V (Figure 4a). Surprisingly, the photocurrent peak in these 2D perovskite structures exhibits strong blue shifts (~55 meV) at high-bias conditions.[41−43] This observation differs from that in typical inorganic MQW structures, which show red shifts from the quantum-confined Stark effect.[44,45] To investigate this further, the spectral photocurrent response is fit using two Gaussian components made up of the broad-band photocurrent (300−475 nm) and narrow exciton photocurrent at 521 nm (Figure S2 in the Supporting Information). While the exciton blue-shifts by 12 nm with increasing applied bias from 0.0 to +2.0 V, its spectral width remains constant. On the other hand, the broad-band photocurrent shows substantial variation in the spectral position as well as spectral width. This could potentially be because more than one mechanism is involved in the generation of photocurrents, for example, BB absorption, CT absorption, etc. Examining the bias dependence of the two contributions (Figure 4b), we find that the threshold bias voltage (at which the photocurrent flips sign) is 0.35 V higher for excitons, emphasizing the different mechanisms involved in creating these photocurrents. In order to better distinguish the different contributions to the photocurrent and their bias dependence, we also use a singular value decomposition analysis (Figure S3 in the Supporting Information), which identifies additional contributions from Stark shifts due to charging, which produces fields on the exciton.

Scanning Photocurrent Microscopy. Global illumination of Al/CHPI/ITO reveals information about the origin of photocurrents, transport (and dynamics) of photogenerated charge carriers, and exciton photocurrent peak tunability. Localized illumination, however, offers insight into the photogeneration and transport mechanisms of photocarriers. Scanning photocurrent microscopy has recently been utilized to study charge transport along 1D semiconductors (such as carbon nanotubes, silicon and Nb_2O_5 nanowires, VO_2, etc.) and at their junctions.[46−48] This technique can also give valuable information related to local band bending and carrier diffusion lengths.[49] Localized low-power-laser (diffraction-limited) irradiation measurements are performed on the lateral photocurrent arrangement (Al/CHPI/Al) shown in Figure 5a (for fabrication, see Methods in the Supporting Information). The 410 nm diode laser (<50 mW) is focused through a 40×

DOI: 10.1021/acsami.5b07026
ACS Appl. Mater. Interfaces 2015, 7, 25227−25236

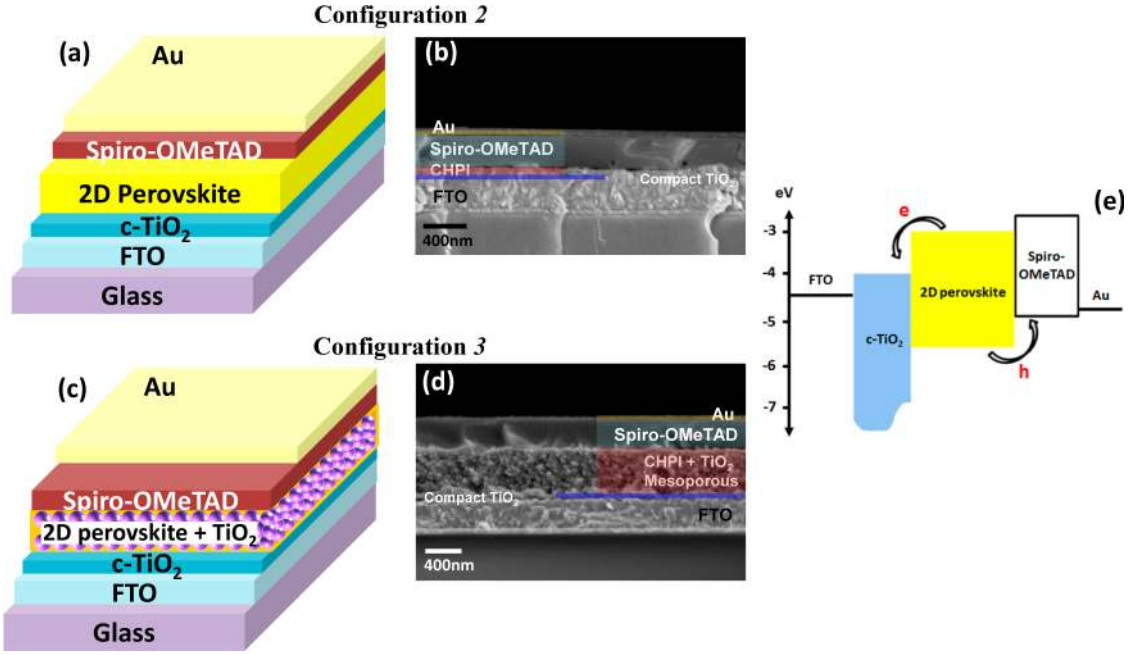

Figure 6. (a) Schematic and (b) cross-sectional SEM of photodetector device configuration **2** [Au/HTL/CHPI/c-TiO_2/FTO]. (c) Schematic and (d) cross-sectional SEM of photodetector device configuration **3** [Au/HTL/CHPI/mp-TiO_2/c-TiO_2/FTO]. (e) Energy diagram of 2D perovskite (CHPI) photodetector configurations **2** and **3** with no bias.

microscope objective to a spot size of ~5 μm. Precise scanning of the laser spot across the two metal contacts is achieved with an XY-piezocontrolled stage, with electrical contacts made using micropositioner probes.

The laser spot spatial position is monitored through a CCD camera, which tracks the observed bright-green luminescence spot (Figure 5b). At an applied potential of +5 V, when the laser spot is scanned from the anode (aluminum; left) to the cathode (aluminum; right) a strong photocurrent is observed only at the *anode*−CHPI interface region (Figure 5c). This photocurrent is still observed at the anode−CHPI interfacial region when the polarities of the aluminum electrodes are exchanged. Additional experiments confirm that the higher photocurrent is collected *only* at the anode−CHPI (+ve terminal) interfacial region.

The photoresponse can be explained by considering the energy band diagram of this Al/CHPI/Al configuration (Figure 5d). At zero bias, the difference in the aluminum metal work function and the electron affinity level of the semiconducting film creates a Schottky potential barrier. When an external bias is applied, band bending occurs according to the respective polarities of the aluminum metal electrodes as well as the type of semiconducting film. At the positively biased side (anode−CHPI interface), the photogenerated electron and hole pairs are separated by a strong local electric field. The electrons move toward the positive terminal (left) and are readily collected. However, holes have to move across the CHPI film to be collected at the negative terminal (right). When we instead consider the case with illumination at the cathode−CHPI interface (right side), the photogenerated holes are readily collected at the negative aluminum terminal (right), while the electrons experience a large barrier and have to diffuse across the film before being collected at the positive terminal (left).

Thus, at positive bias there is always a unidirectional flow of carriers, irrespective of the illumination position. Despite the relatively low diffusion rate of the holes, the photocurrents at the positive terminal are always higher than those at the negative terminal (Figure 5d), which occurs when the semiconducting channel is of the p-type.[47] Therefore, these scanning photocurrent microscopy measurements imply that this CHPI 2D perovskite is a p-type semiconductor. Mitzi et al. used extensive varieties of related 2D IO perovskites (tin- and lead-based) in transistors and also found them to be in the p-type,[11,12,50,51] as indeed is also the parent PbI_2.[50]

Effect of the Electron- and Hole-Transport Layers. On the basis of our observations, we conclude that the energy stored as strongly bound excitons in this 2D perovskite may, nevertheless, be harvested in the presence of a suitable interface. This behavior is conceptually similar to that utilized by photovoltaics based on organic semiconductors and dyes: pristine organic films achieve external quantum efficiency (EQE) of the order of 0.1% because of the low probability of spontaneous thermal dissociation of excitons.[52,53] By contrast, organic heterojunctions introducing a suitable electric field or potential step, achieved by pairing the organic with a complementary metal or semiconductor layer, exhibit relatively high exciton dissociation efficiencies.[54] We therefore adapt our design to introduce two carrier-selective, nonmetallic interfaces (p-type spiro-OMeTAD and n-type TiO_2), both of which should have the capability of dissociating a bound e−h pair without introducing image-dipole or plasmon quenching. To observe the effects of electron- and hole-transport materials on charge carriers in the 2D perovskite, the photodetector configurations **2** and **3** are studied. Parts a and c of Figure 6 show the schematic layer structures and parts b and d of Figure 6 the corresponding cross-sectional SEM images of both configurations (**2** and **3**). In configuration **2**, CHPI coats a compact TiO_2 (c-TiO_2) electron-transport layer (ETL) and is overcoated with spiro-OMeTAD as the hole-transport layer (HTL) and gold to produce heterojunction configuration [Au/HTL/CHPI/c-TiO_2/FTO] (see Methods in the Supporting Information).[4,5] In configuration **3**, an additional 500 nm thick

DOI: 10.1021/acsami.5b07026
ACS Appl. Mater. Interfaces 2015, 7, 25227−25236

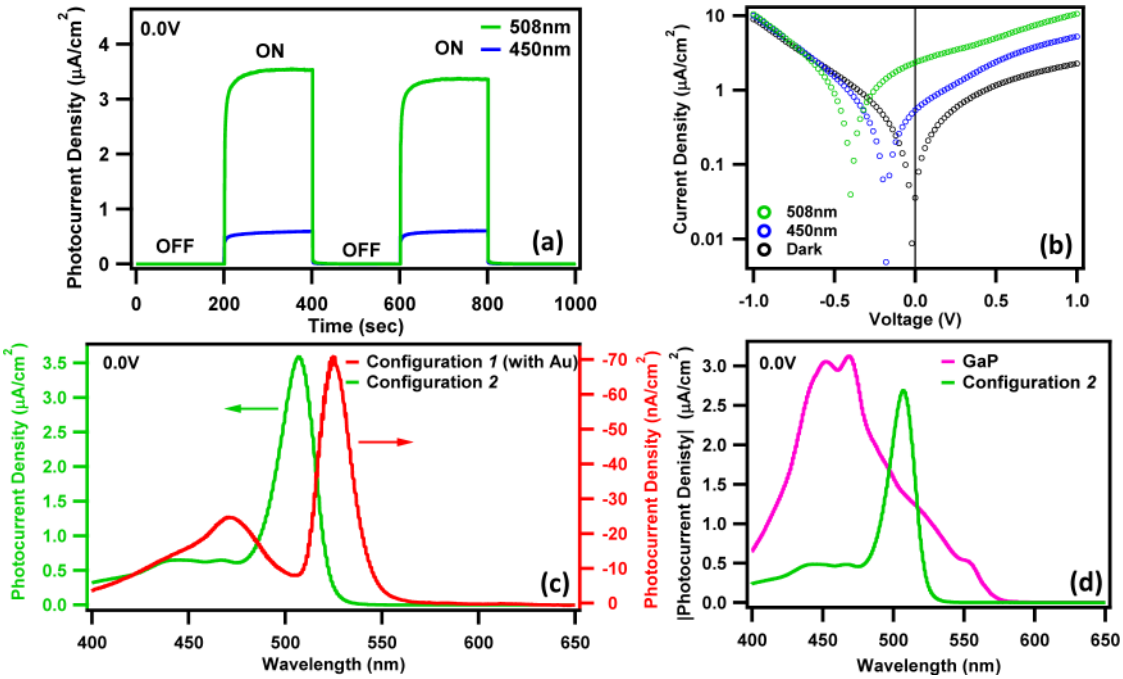

Figure 7. (a) Transient photocurrent response of configuration **2** under periodic ON/OFF illumination of 450 and 508 nm light at 0 V bias. (b) *I*–*V* characteristics of configuration **2** under 450 nm, 508 nm exposure, and dark conditions. (c) Photocurrent spectrum of configuration **2** measured at 0 V bias. The photocurrent spectrum of configuration **1** (with gold top electrode) is added for comparison. (d) Comparison of the photocurrent spectral response of configuration **2** with a commercially available GaP photodiode.

mesoporous TiO_2 (mp-TiO_2) layer is spun onto the c-TiO_2 layer before infiltrating with CHPI [Au/HTL/CHPI/mp-TiO_2/c-TiO_2/FTO].[1,2] These structures are inspired by recent progress in the field of 3D perovskite-based solar cells, where device optimization has led to PCEs exceeding 15% in just a few years.[1−4]

The transient photocurrent of configuration **2** recorded at two different excitation wavelengths, 450 and 508 nm, corresponding respectively to BB and exciton transitions, shows a prompt and strongly enhanced photocurrent compared to the pristine configuration **1** (Figure 7a). After many ON/OFF cycles, only a slight degradation in the photocurrent magnitude is observed. At 0 V bias, the photocurrent corresponding to exciton transitions (at 508 nm) is larger by a factor of 7 compared to the photocurrent obtained for BB transitions (at 450 nm). The photocurrent spectral response, recorded for the visible region of the spectra, again shows significant enhancement in the narrow exciton band (peaked at 508 nm) compared to the broad-band features associated with BB transitions. Thus, the addition of carrier-transport layers does not alter this surprising strength of exciton photocurrent contributions. The narrow exciton photocurrent peak possesses a fwhm of ∼21 nm, which shows that, even with the presence of both ETL and HTL, the 2D perovskite in the photodetector configuration maintains the MQW structures, resulting in excitonic features but still facilitating dissociation of the tightly bound e−h pairs. The current−voltage (*I*–*V*) curves represent typical semiconductor diode-like characteristics with significant enhancement in the generated photocurrent under 450 and 508 nm illumination (Figure 7b). The shifts in *I*–*V* curves along the negative voltage axis indicate the generation of photovoltage upon illumination. The exciton photocurrent peak shows a blue shift of 17 nm compared to configuration **1** (fabricated with a top gold electrode; Figure 7c). This blue-shifted exciton photocurrent peak better matches the absorption spectrum of CHPI, which has an exciton peak at 506 nm (Figure 2a). Hence, this suggests that the large exciton photocurrent now comes from the bulk CHPI within the full thickness of the device.

The photodetector in configuration **2** is compared with a commercial GaP photodiode (FGAP71, Thorlabs). The as-prepared CHPI-based photodetector configuration **2** was not encapsulated with any sealing agent or epoxy and all measurements were performed in air. The photocurrent spectral response of configuration **2** shows an efficiency comparable to that of the GaP photodiode (Figure 7d). Thus, such 2D perovskite-based photodetectors could be suited to specific detector applications at wavelengths of around 500 nm. Because previous work reports wide exciton tunability in these perovskites (achieved by compositional substitutions of cations and anions as well as varied layer stackings and variation of the organic moieties; Figure S4 in the Supporting Information),[25,28,29] photodetectors could be fabricated with appropriate 2D perovskite materials for many specific target spectral regions.

To further explore interplane exciton and carrier transport in 2D perovskite-based photodetectors, configuration **3** is studied in which a thick layer (∼500 nm) of CHPI/mp-TiO_2 is sandwiched between the c-TiO_2 and spiro-OMeTAD layers (Figure 6c). The SEM cross-sectional image of configuration **3** (Figure 6d) shows no clear CHPI layer between mp-TiO_2 and spiro-OMeTAD, indicating that the 2D perovskite is well dispersed in the mp-TiO_2 layer. Recent studies on 3D perovskite-based solar cells demonstrate that $CH_3NH_3PbI_3$ forms closely packed networks of perovskite cubic unit cells around TiO_2 nanoparticle scaffolds, facilitating extraction of photogenerated electrons to TiO_2, with holes being transferred to spiro-OMeTAD.[1] The situation for layered 2D perovskites is

DOI: 10.1021/acsami.5b07026
ACS Appl. Mater. Interfaces 2015, 7, 25227−25236

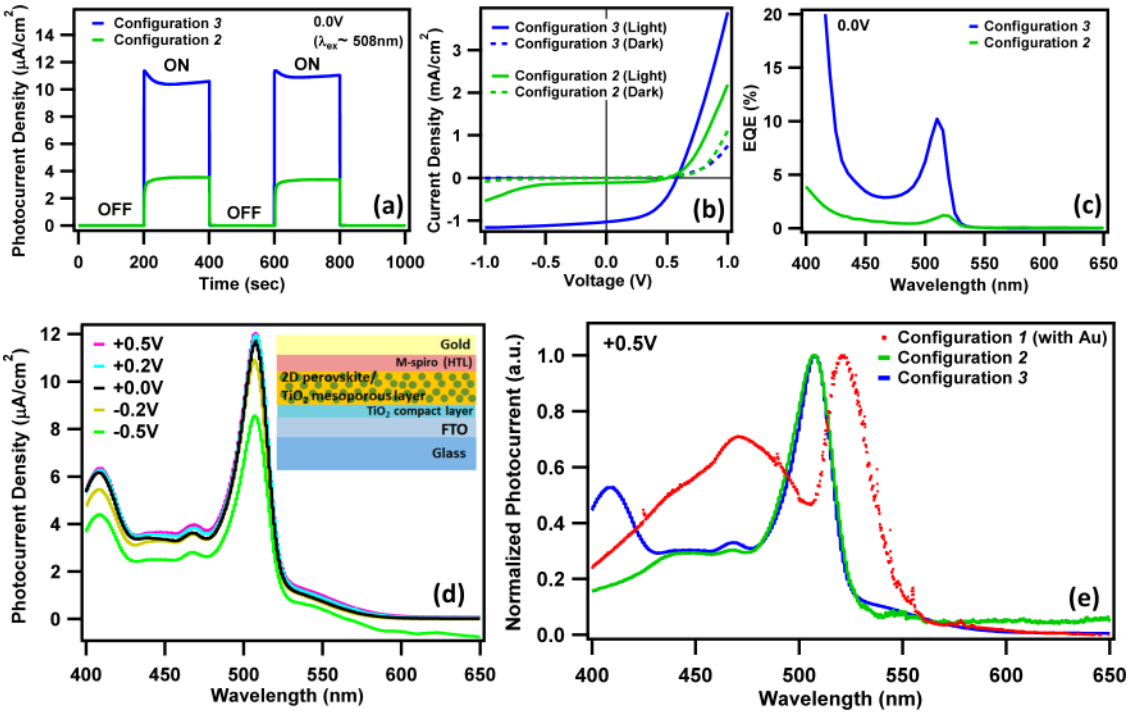

Figure 8. (a) Transient photocurrent response of configurations **2** and **3** under periodic ON/OFF illumination at 508 nm with 0 V bias. (b) $I-V$ characteristics of heterojunction photodetector configurations **2** and **3** measured in the dark (dashed line) and under 100 mW cm^{-2} (AM1.5G) photon flux (solid line) [note: the bias polarity is inverted compared to previous measurements to get a conventional $I-V$ curve]. (c) Corresponding EQE spectra showing improvement in the efficiency at exciton wavelengths in configuration **3**. (d) Room-temperature photocurrent spectra of configuration **3** recorded under different applied potentials (inset shows schematic). (e) Comparison of normalized photocurrent spectra of configurations **1** (with gold top electrodes), **2**, and **3**, at +0.5 V bias.

expected to be similar, with the TiO_2 nanoparticles not disturbing the self-assembled alternate stacking of IO layers. This is further confirmed by glancing-angle X-ray diffraction (GAXRD) spectra of configuration **3** without top spiro-OMeTAD and gold contacts. The X-ray diffraction pattern shows the dominance of *c*-axis-oriented (00*l*) planes, signifying the presence of a strong layering arrangement of inorganic and organic sheets (Figure S5 in the Supporting Information). The crystallite size estimated from Scherrer's formula using the angular width of the narrow (001) characteristic peak occurring at $2\theta = 5.12°$ is found to be 83 nm, which is actually much larger than that for a CHPI film spin-coated onto glass (12 nm). The crystallite size of the perovskite depends on the porosity of the mesoporous scaffold, which can be optimized by varying the nanoparticle size.[55]

The photocurrent measured for configuration **3** under 508 nm illumination at 0 V is 3 times larger than that for configuration **2**. The transient photocurrent shown in Figure 8a is recorded under periodic illumination at 508 nm for several cycles under zero bias conditions. The photocurrent rises very rapidly (submilliseconds) during the transition from OFF to ON states and rapidly decreases to zero as soon as the light turns off, much faster than that for configuration **2**. These results are highly reproducible, and the photocurrent magnitude is found to be completely stable over many ON/OFF cycles, in contrast to configuration **2**. After the fast anodic spike, the photocurrent slightly decays with a slow time constant of ~20 s before settling to a stable photocurrent. This slow decay in the photocurrent is attributed to the accumulation of excess electrons on the TiO_2 surfaces. Rather than being trapped or extracted, these electrons undergo competitive recombination with the holes available at the nearest site in the perovskite. Once the equilibration of competitive separation and recombination of electron–hole pairs is attained, the photocurrent remains constant.

The $I-V$ characteristics of both configurations **2** and **3** are recorded at room temperature under simulated AM1.5G solar illumination and show typical photodiode behavior. The open-circuit voltages (V_{oc}) for these devices are 0.51 and 0.58 V for configurations **2** and **3**, respectively (Figure 8b). The effect of the mp-TiO_2 layer is to enhance the short-circuit current density (J_{sc}) roughly 9-fold, from 0.11 to 1.03 mA cm^{-2}. Configuration **3** shows a PCE of 0.3%, which is 11 times higher than that of configuration **2** (0.027%).

Room-temperature EQE measurements were performed for a wide spectral range and are compared in Figure 8c. Although the EQE values for configuration **3** are found to be higher than those for configuration **2** across the whole spectrum range, this enhancement is stronger at the exciton wavelength (508 nm) with 10% EQE, which is 8 times higher, and in the BB transition region, with 36% EQE, which is 9 times higher. The overall improvement in the EQE of configuration **3** can be attributed to the role of spherical TiO_2 nanoparticles forming mesoporous structures of high aspect ratios, which promote electron transfer between PbI_4 layers as well as increased optical scattering, resulting in this significant enhancement in the device performance.[56,57] Moreover, charge transport within the perovskite is improved because of the larger grain size, reducing the number of grain boundaries and making it possible to have single grains span the space between two TiO_2 nanoparticles. These results thus show the role of TiO_2 nanoparticles in improving the photocurrent efficiencies, which remain a source

DOI: 10.1021/acsami.5b07026
ACS Appl. Mater. Interfaces 2015, 7, 25227–25236

of considerable controversy in solar cells based on 3D perovskites.[58]

The bias dependencies of the photocurrent spectral response for both configurations **2** and **3** are studied at room temperature (Figure 8d,e). At zero bias, both configurations exhibit a strong exciton photocurrent peak at 508 nm. Unlike configuration **1**, changing the applied bias does not change the exciton photocurrent peak position (508 nm) for configurations **2** and **3**. The overall comparison between the normalized photocurrent spectra for all three structures (Figure 8e) shows that configuration **1** displays different spectral responses at both exciton and BB transitions, likely because of the rate-determining collection at the Schottky aluminum−gold contact, which has high space-charge fields. The additional peak around 400 nm in configuration **3** is likely due to the intrinsic photocurrent response of the anatase phase TiO_2 nanoparticles.[59,60] Similar enhancements are seen for another 2D perovskite when the TiO_2 nanoparticles are inserted into the active layer (Figure S6 in the Supporting Information).

CONCLUSION

This investigation of the room-temperature photocurrent properties of 2D IO perovskites reveals that excitons strongly contribute to the photocurrents despite possessing binding energies more than 10-fold larger than the thermal energies. The p-type CHPI liberates photocarriers at metallic Schottky aluminum contacts, but charging slows down the photoresponse. In contrast, using ETL and HTL enhances the extracted photocurrents by 100-fold, and a further 10-fold gain is found when mixing TiO_2 nanoparticles directly into the perovskite layers, although the 2D exciton layers are not significantly disrupted. We thus conclude that exciton dissociation must occur within strong local electric fields, at the material interfaces, or at crystal grain boundaries. We also find that carrier transport between the >1-nm-spaced QW sheets is far more efficient in these 2D materials than was expected from previous considerations, probably because of rapid lateral transport to grain boundaries or the TiO_2 nanoparticles. These results show that strong excitonic materials may be useful as photovoltaic materials despite high binding energies and provide useful evidence in the understanding of the related 3D perovskites.

ASSOCIATED CONTENT

Supporting Information

The Supporting Information is available free of charge on the ACS Publications website at DOI: 10.1021/acsami.5b07026.

Figures S1−S6, figure-related details, and details of the experimental methods (PDF)

AUTHOR INFORMATION

Corresponding Authors

*E-mail: sa754@cam.ac.uk.
*E-mail: prakash@physics.iitd.ac.in.
*E-mail: jjb12@cam.ac.uk.

Author Contributions

The manuscript was written through equal contributions of all authors and all authors have given approval to the final version of the manuscript.

Notes

The authors declare no competing financial interest.

ACKNOWLEDGMENTS

This work is part of the High-Impact Research scheme of IIT Delhi, DST project (Government of India), DST-FIST (Government of India), and U.K.−India Education and Research Initiative (UKIERI) programmes. This work was supported by EPSRC Grants EP/K028510/1, EP/G060649/1, EP/G037221/1, EP/H007024/1, EP/L027151/1, and EP/L015978/1, the Cambridge NanoDTC, and ERC LINASS 320503.

REFERENCES

(1) Lee, M. M.; Teuscher, J.; Miyasaka, T.; Murakami, T. N.; Snaith, H. J. Efficient Hybrid Solar Cells Based on Meso-Superstructured Organometal Halide Perovskites. *Science* **2012**, *338*, 643−647.

(2) Kim, H. S.; Lee, C. R.; Im, J. H.; Lee, K. B.; Moehl, T.; Marchioro, A.; Moon, S. J.; Humphry-Baker, R.; Yum, J. H.; Moser, J. E.; Gratzel, M.; Park, N. G. Lead Iodide Perovskite Sensitized All-Solid-State Submicron Thin Film Mesoscopic Solar Cell with Efficiency Exceeding 9%. *Sci. Rep.* **2012**, *2*, 591-1−591-7.

(3) Zhou, H.; Chen, Q.; Li, G.; Luo, S.; Song, T.; Duan, H.-S.; Hong, Z.; You, J.; Liu, Y.; Yang, Y. Interface Engineering of Highly Efficient Perovskite Solar Cells. *Science* **2014**, *345*, 542−546.

(4) Green, M. A.; Ho-Baillie, A.; Snaith, H. J. The Emergence of Perovskite Solar Cells. *Nat. Photonics* **2014**, *8*, 506−514.

(5) Liu, D.; Kelly, T. L. Perovskite Solar Cells with a Planar Heterojunction Structure Prepared Using Room-Temperature Solution Processing Techniques. *Nat. Photonics* **2013**, *8*, 133−138.

(6) Habisreutinger, S.; Leijtens, T.; Eperon, G.; Stranks, S.; Nicholas, R.; Snaith, H. Carbon Nanotube/Polymer Composites as a Highly Stable Hole Collection Layer in Perovskite Solar Cells. *Nano Lett.* **2014**, *14*, 5561−5568.

(7) Leijtens, T.; Eperon, G. E.; Pathak, S.; Abate, A.; Lee, M. M.; Snaith, H. J. Overcoming Ultraviolet Light Instability of Sensitized TiO_2 with Meso-Superstructured Organometal Tri-Halide Perovskite Solar Cells. *Nat. Commun.* **2013**, *4*, 2885-1−2885-8.

(8) D'Innocenzo, V.; Grancini, G.; Alcocer, M. J. P.; Kandada, A. R. S.; Stranks, S. D.; Lee, M. M.; Lanzani, G.; Snaith, H. J.; Petrozza, A. Excitons Versus Free Charges in Organo-Lead Tri-Halide Perovskites. *Nat. Commun.* **2014**, *5*, 3586-1−3586-6.

(9) Mitzi, D. B. Synthesis, Structure, and Properties of Organic−Inorganic Perovskites and Related Materials. In *Progress in Inorganic Chemistry*; Karlin, K. D., Ed.; Wiley-Interscience: New York, 2007; Vol. *48*, pp 1−121.

(10) Pradeesh, K.; Rao, K. N.; Vijaya Prakash, G. Synthesis, Structural, Thermal and Optical Studies of Inorganic-Organic Hybrid Semiconductors, R-PbI_4. *J. Appl. Phys.* **2013**, *113*, 083523.

(11) Kagan, C.; Mitzi, D.; Dimitrakopoulos, C. Organic-Inorganic Hybrid Materials as Semiconducting Channels in Thin-Film Field-Effect Transistors. *Science* **1999**, *286*, 945−947.

(12) Mitzi, D. B.; Wang, S.; Feild, C. A.; Chess, C. A.; Guloy, A. M. Conducting Layered Organic-inorganic Halides Containing (110)-Oriented Perovskite Sheets. *Science* **1995**, *267*, 1473−1476.

(13) Papavassiliou, G. C. Three- and Low-Dimensional Inorganic Semiconductors. *Prog. Solid State Chem.* **1997**, *25*, 125−270.

(14) Mitzi, D. Templating and Structural Engineering in Organic−inorganic Perovskites. *J. Chem. Soc., Dalton Trans.* **2001**, *1*, 1−12.

(15) Calabrese, J.; Jones, N. L.; Harlow, R. L.; Herron, N.; Thorn, D. L.; Wang, Y. Preparation and Characterization of Layered Lead Halide Compounds. *J. Am. Chem. Soc.* **1991**, *113*, 2328−2330.

(16) Muljarov, E. A.; Tikhodeev, S. G.; Gippius, N. A.; Ishihara, T. Excitons in Self-Organized Semiconductor/insulator Superlattices: PbI-Based Perovskite Compounds. *Phys. Rev. B: Condens. Matter Mater. Phys.* **1995**, *51*, 14370−14378.

(17) Takeda, J.; Ishihara, T.; Goto, T. Low Energy Tail of the Exciton Luminescence Band in 2H-Pbi_2 and its Relation To Urbach Rule. *Solid State Commun.* **1985**, *56*, 101−103.

DOI: 10.1021/acsami.5b07026
ACS Appl. Mater. Interfaces 2015, 7, 25227−25236

(18) Ishihara, T.; Takahashi, J.; Goto, T. Exciton State in Two-Dimensional Perovskite Semiconductor $(C_{10}H_{21}NH_3)_2PbI_4$. *Solid State Commun.* **1989**, *69*, 933−936.
(19) Ishihara, T.; Takahashi, J.; Goto, T. Optical Properties due to Electronic Transitions in Two-Dimensional Semiconductors $(C_nH_{2n+1}NH_3)_2PbI_4$. *Phys. Rev. B: Condens. Matter Mater. Phys.* **1990**, *42*, 11099−11107.
(20) Goto, T.; Makino, H.; Yao, T.; Chia, C. H.; Makino, T.; Segawa, Y.; Mousdis, G. A.; Papavassiliou, G. C. Localization of Triplet Excitons and Biexcitons in the Two-Dimensional Semiconductor $(CH_3C_6H_4CH_2NH_3)_2PbBr_4$. *Phys. Rev. B: Condens. Matter Mater. Phys.* **2006**, *73*, 115206-1−115206-5.
(21) Shimizu, M.; Fujisawa, J. I.; Ishi-Hayase, J. Influence of Dielectric Confinement on Excitonic Nonlinearity in Inorganic-Organic Layered Semiconductors. *Phys. Rev. B: Condens. Matter Mater. Phys.* **2005**, *71*, 205306−205309.
(22) Shimizu, M.; Gippius, N. A.; Tikhodeev, S. G.; Ishihara, T. Coulomb Correction to the Dressed Exciton in an Inorganic-Organic Layered Semiconductor: Detuning Dependence of the Stark Shift. *Phys. Rev. B: Condens. Matter Mater. Phys.* **2004**, *69*, 155201-1−155201-5.
(23) Vijaya Prakash, G.; Pradeesh, K.; Ratnani, R.; Saraswat, K.; Light, M. E.; Baumberg, J. J. Structural and Optical Studies of Local Disorder Sensitivity in Natural Organic-Inorganic Self-Assembled Semiconductors. *J. Phys. D: Appl. Phys.* **2009**, *42*, 185405-1−185405-7.
(24) Dwivedi, V. K.; Baumberg, J. J.; Prakash, G. V. Direct Deposition of Inorganic-organic Hybrid Semiconductors and Their Template-Assisted Microstructures. *Mater. Chem. Phys.* **2013**, *137*, 941−946.
(25) Ahmad, S.; Prakash, G. V. Two-Step Fabrication of R-$PbI_{4(1-Y)}Br_{4y}$ type Light Emitting Inorganic-Organic Hybrid Photonic Structures. *Opt. Mater. Express* **2014**, *4*, 101−110.
(26) Ahmad, S.; Kanaujia, P. K.; Niu, W.; Baumberg, J. J.; Vijaya Prakash, G. In Situ Intercalation Dynamics in Inorganic−Organic Layered Perovskite Thin Films. *ACS Appl. Mater. Interfaces* **2014**, *6*, 10238−10247.
(27) Pradeesh, K.; Baumberg, J. J.; Prakash, G. V. In Situ Intercalation Strategies for Device-Quality Hybrid Inorganic-Organic Self-Assembled Quantum Wells. *Appl. Phys. Lett.* **2009**, *95*, 033309-1−033309-3.
(28) Ahmad, S.; Baumberg, J. J.; Vijaya Prakash, G. Structural Tunability and Switchable Exciton Emission in Inorganic-Organic Hybrids with Mixed Halides. *J. Appl. Phys.* **2013**, *114*, 233511-1−233511-8.
(29) Ahmad, S.; Prakash, G. V. Strong Room-Temperature UV to Red Excitons from Inorganic Organic Layered Perovskites, $(R\text{-}NH_3)_2MX_4$ ($M = Pb^{2+}$, Sn^{2+}, Hg^{2+}; $X = I^-$, Br^-). *J. Nanophotonics* **2014**, *8*, 083892-1−083892-12.
(30) Pradeesh, K.; Baumberg, J. J.; Prakash, G. V. Strong Exciton-Photon Coupling in Inorganic-Organic Multiple Quantum Wells Embedded Low-Q Microcavity. *Opt. Express* **2009**, *17*, 22171−22178.
(31) Bube, R. H. *Photoelectronic Properties of Semiconductors*, 1st ed; Cambridge University Press: Cambridge, U.K., 1992.
(32) Moss, T. Photoconductivity. *Rep. Prog. Phys.* **1965**, *28*, 15−60.
(33) Umlauff, M.; Hoffmann, J.; Kalt, H.; Langbein, W.; Hvam, J. M.; Scholl, M.; Söllner, J.; Heuken, M.; Jobst, B.; Hommel, D. Direct Observation of Free-Exciton Thermalization in Quantum-Well Structures. *Phys. Rev. B: Condens. Matter Mater. Phys.* **1998**, *57*, 1390−1393.
(34) Mitzi, D. B.; Dimitrakopoulos, C. D.; Rosner, J.; Medeiros, D. R.; Xu, Z.; Noyan, C. Hybrid Field Effect Transistor Based on a Low Temperature Melt Processed Channel Layer. *Adv. Mater.* **2002**, *14*, 1772−1776.
(35) Wyckoff, R. W. G. *Crystal Structures*, 2nd ed.; Wiley-Interscience: New York, 1963; Vol. *1*.
(36) Billing, D. G.; Lemmerer, A. Poly[bis[2-(1-cyclohexenyl)-ethylammonium] di-μ-iodo-diodoplumbate(II)]. *Acta Crystallogr., Sect. C: Cryst. Struct. Commun.* **2006**, *62*, m269−m271.
(37) Ferreira da Silva, A.; Veissid, N.; An, C.; Pepe, I.; Barros de Oliveira, N.; Batista da Silva, A. Optical Determination of the Direct Bandgap Energy of Lead Iodide Crystals. *Appl. Phys. Lett.* **1996**, *69*, 1930−1932.
(38) Hong, X.; Ishihara, T.; Nurmikko, A. V. Photoconductivity and Electroluminescence in Lead Iodide Based Natural Quantum Well Structures. *Solid State Commun.* **1992**, *84*, 657−661.
(39) Papavassiliou, G. C.; Mousdis, G. A.; Koutselas, I. B.; Papaioannou, G. J. Excitonic Bands in the Photoconductivity Spectra of Some Organic-Inorganic Hybrid Compounds Based on Metal Halide Units. *Int. J. Mod. Phys. B* **2001**, *15*, 3727−3731.
(40) Monte, A. F. G; Finley, J. J.; Whittaker, D. M.; Itskevitch, I.; Mowbray, D. J.; Skolnick, M. S.; Sales, F. V.; Hopkins, M. Non-Linear Effects on the Power Dependent Photocurrent of Self-Assembled InAs/GaAs Quantum Dots. *Microelectron. J.* **2003**, *34*, 667−669.
(41) Miller, D. A. B.; Chemla, D. S.; Damen, T. C.; Gossard, A. C.; Wiegmann, W.; Wood, T. H.; Burrus, C. A. Band-Edge Electroabsorption in Quantum Well Structures: The Quantum-Confined Stark Effect. *Phys. Rev. Lett.* **1984**, *53*, 2173−2176.
(42) Gug, R. K.; Hagston, W. E. Large Blue Shifts Induced by the Quantum Confined Stark Effect in Asymmetric Quantum Wells. *Appl. Phys. Lett.* **1998**, *73*, 1547−1549.
(43) Mohite, A.; Lin, J. T.; Sumanasekera, G.; Alphenaar, B. W. Field-Enhanced Photocurrent Spectroscopy of Excitonic States in Single-Wall Carbon Nanotubes. *Nano Lett.* **2006**, *6*, 1369−1373.
(44) Kuo, Y. H.; Lee, Y.; Ge, Y.; Ren, S.; Roth, J.; Kamins, T.; Miller, D.; Harris, J. S., Jr. Quantum-Confined Stark Effect in Ge/SiGe Quantum Wells on Si for Optical Modulators. *IEEE J. Sel. Top. Quantum Electron.* **2006**, *12*, 1503−1513.
(45) Goossen, K. W.; Caridi, E. A.; Chang, T. Y.; Stark, J. B.; Miller, D.; Morgan, R. A. Observation of Room Temperature Blue Shift and Bistability in a Strained InGaAs GaAs < 111> Self Electro Optic Effect Device. *Appl. Phys. Lett.* **1990**, *56*, 715−717.
(46) Kasirga, T. S.; Sun, D.; Park, J. H.; Coy, J. M.; Fei, Z.; Xu, X.; Cobden, D. H. Photoresponse of a Strongly Correlated Material Determined by Scanning Photocurrent Microscopy. *Nat. Nanotechnol.* **2012**, *7*, 723−727.
(47) Tamang, R.; Varghese, B.; Mhaisalkar, S. G.; Tok, E. S.; Sow, C. H. Probing the Photoresponse of Individual Nb2O5 Nanowires with Global and Localized Laser Beam Irradiation. *Nanotechnology* **2011**, *22*, 115202-1−115202-9.
(48) Graham, R.; Miller, C.; Oh, E.; Yu, D. Electric Field Dependent Photocurrent Decay Length in Single Lead Sulfide Nanowire Field Effect Transistors. *Nano Lett.* **2011**, *11*, 717−722.
(49) Friel, I.; Thomidis, C.; Fedyunin, Y.; Moustakas, T. D. Investigation of Excitons in AlGaN/GaN Multiple Quantum Wells by Lateral Photocurrent and Photoluminescence Spectroscopies. *J. Appl. Phys.* **2004**, *95*, 3495−3502.
(50) Mitzi, D. B.; Chondroudis, K.; Kagan, C. R. Organic-Inorganic Electronics. *IBM J. Res. Dev.* **2001**, *45* (1), 29−45.
(51) Mitzi, D. B.; Feild, C. A.; Harrison, W. T. A.; Guloy, A. M. Conducting Tin Halides with a Layered Organic-Based Perovskite Structure. *Nature* **1994**, *369*, 467−469.
(52) Tang, C. W.; Albrecht, A. C. Chlorophyll-*a* Photovoltaic Cells. *Nature* **1975**, *254*, 507−509.
(53) Kallmann, H.; Pope, M. Photovoltaic Effect in Organic Crystals. *J. Chem. Phys.* **1959**, *30*, 585−586.
(54) Park, S. H.; Roy, A.; Beaupré, S.; Cho, S.; Coates, N.; Moon, J. S.; Moses, D.; Leclerc, M.; Lee, K.; Heeger, A. J. Bulk Heterojunction Solar Cells with Internal Quantum Efficiency Approaching 100%. *Nat. Photonics* **2009**, *3*, 297−302.
(55) Elgh, B.; Yuan, N.; Cho, H.; Magerl, D.; Philipp, M.; Roth, S.; Yoon, K.; Müller-Buschbaum, P.; Terasaki, O.; Palmqvist, A. Controlling Morphology, Mesoporosity, Crystallinity, and Photocatalytic Activity of Ordered Mesoporous TiO_2 Films Prepared at Low Temperature. *APL Mater.* **2014**, *2*, 113313-1−113313-13.
(56) Shao, W.; Gu, F.; Li, C.; Lu, M. Interfacial Confined Formation of Mesoporous Spherical TiO2 Nanostructures with Improved

DOI: 10.1021/acsami.5b07026
ACS Appl. Mater. Interfaces 2015, 7, 25227−25236

Photoelectric Conversion Efficiency. *Inorg. Chem.* **2010**, *49*, 5453−5459.
(57) Ito, S.; Zakeeruddin, S. M.; HumphryBaker, R.; Liska, P.; Charvet, R.; Comte, P.; Nazeeruddin, M. K.; Péchy, P.; Takata, M.; Miura, H.; Uchida, S.; Grätzel, M. High Efficiency Organic Dye Sensitized Solar Cells Controlled by Nanocrystalline TiO_2 Electrode Thickness. *Adv. Mater.* **2006**, *18* (9), 1202−1205.
(58) Liu, M.; Johnston, M. B.; Snaith, H. J. Efficient Planar Heterojunction Perovskite Solar Cells by Vapour Deposition. *Nature* **2013**, *501*, 395−398.
(59) Hidalgo, M. C.; Aguilar, M.; Maicu, M.; Navío, J. A.; Colón, G. Hydrothermal Preparation of Highly Photoactive TiO_2 Nanoparticles. *Catal. Today* **2007**, *129*, 50−58.
(60) Hossain, F. M.; Sheppard, L.; Nowotny, J.; Murch, G. E. Optical Properties of Anatase and Rutile Titanium Dioxide: Ab Initio Calculations for Pure and Anion-Doped Material. *J. Phys. Chem. Solids* **2008**, *69*, 1820−1828.

DOI: 10.1021/acsami.5b07026
ACS Appl. Mater. Interfaces 2015, 7, 25227−25236